Biochimica et Biophysica Acta 1858 (2016) 813–823

Contents lists available at ScienceDirect

Biochimica et Biophysica Acta

journal homepage: www.elsevier.com/locate/bbamem

A computational study of ion current modulation in hVDAC3 induced by disulfide bonds

Carlo Guardiani [a], Loredana Leggio [b,c], Mariano Andrea Scorciapino [a,d], Vito de Pinto [b,c], Matteo Ceccarelli [a,e,*]

[a] Istituto Officina dei Materiali, Consiglio Nazionale delle Ricerche (CNR-IOM), UOS, Cagliari, Italy
[b] Department of Biomedical and Biotechnological Sciences, BIOMETEC, University of Catania, Italy
[c] National Institute for Biomembranes and Biosystems, Section of Catania, viale A. Doria 6, 95125 Catania, Italy
[d] Department of Biomedical Sciences, Biochemistry Unit, University of Cagliari, Italy
[e] Department of Physics, University of Cagliari, Cagliari, Italy

ARTICLE INFO

Article history:
Received 1 September 2015
Received in revised form 5 December 2015
Accepted 19 January 2016
Available online 22 January 2016

Keywords:
Voltage dependent anion channels
Cysteine oxidation states
Molecular dynamics
Structural bioinformatics
Neural networks
Conductance

ABSTRACT

The human VDAC channel exists in three isoforms characterized by high sequence homology and structural similarity. Yet the function and mode of action of hVDAC3 are still elusive. The presence of six surface cysteines exposed to the oxidizing environment of the mitochondrial inter-membrane space suggests the possible establishment of intramolecular disulfide bonds. Two natural candidates for disulfide bridge formation are Cys2 and Cys8 that, located on the flexible N-terminal domain, can easily come in contact. A third potentially important residue is Cys122 that is close to Cys2 in the homology model of VDAC3. Here we analyzed the impact of SS bonds through molecular dynamics simulations of derivatives of hVDAC3 (dubbed SS-2-8, SS-2-122, SS-8-122) including a single disulfide bond. Simulations showed that in SS-8-122, the fragment 1-7 crosses the top part of the barrel partially occluding the pore and causing a 20% drop of conductance. In order to identify other potential channel-occluding disulfide bonds, we used a set of neural networks and structural bioinformatics algorithms, after filtering with the steric constraints imposed by the 3D-structure. We identified other three species, namely SS-8-65, SS-2-36 and SS-8-36. While the conductance of SS-8-65 and SS-2-36 is about 30% lower than that of the species without disulfide bonds, the conductance of SS-8-36 was 40–50% lower. The results show how VDAC3 is able to modulate its pore size and current by exploiting the mobility of the N-terminal and forming, upon external stimuli, disulfide bridges with cysteine residues located on the barrel and exposed to the inter-membrane space.

1. Introduction

The Voltage-Dependent Anion Channel (VDAC) is the most abundant integral membrane protein of the mitochondrial outer membrane and it is responsible for the exchange of adenosine nucleotides, sugars and inorganic ions between the mitochondrial and cytoplasmic compartments [1–3]. Three different VDAC isoforms have been characterized in higher eukaryotes, encoded by three separate genes [4]. These genes feature a remarkably similar organization comprising the same number of exons sharing exactly the same size. The genetic similarity is suggestive of a common evolutionary origin [5]. It is widely accepted that VDAC3 is the oldest protein of the family. The divergence between VDAC3 and VDAC1/2 has been estimated to occur about 365 millions years ago, while the divergence between VDAC1 and VDAC2 occurred more recently, about 289 millions of years ago. The phylogenetic tree, therefore, suggests a high degree of structural and functional similarity between VDAC1 and VDAC2, and a weaker correlation between the features of these proteins and those of VDAC3.

Three experimental three-dimensional structures of mouse and human VDAC1 isoform have been recently determined by X-ray crystallography and NMR [6–8]. These analyses revealed a beta-barrel motif with 19 amphipathic beta strands. Each strand features a regular alternation of hydrophilic and hydrophobic residues, the former pointing to the water-accessible lumen of the channel and the latter interacting with the apolar membrane environment. The barrel is made by a regular antiparallel organization of the beta-strands, but the pattern is interrupted by the parallel pairing of strands 1 and 19. This organization is peculiar of the VDAC family and contrasts with the rule of the even number of strands pertaining to bacterial porins [9]. The VDAC structure is completed by an N-terminal tail located inside the pore. However, the exact position and local structure of this segment are still elusive since these features are different in the available X-ray and NMR structures. For the sake of completeness, it must be reported that this structural model of the VDAC protein has been recently questioned by Colombini [10]. One of the main reasons inspiring the criticism for the 19-stranded model is the consideration that the artificial folding procedure used to

* Corresponding author at: Istituto Officina dei Materiali, Consiglio Nazionale delle Ricerche (CNR-IOM), UOS, Cagliari, Italy.
E-mail address: matteo.ceccarelli@dsf.unica.it (M. Ceccarelli).

http://dx.doi.org/10.1016/j.bbamem.2016.01.013
0005-2736/

prepare enough material for the crystallization might produce two or more populations of stable VDAC structures and the proposed crystallized structure might be just one of these alternatives.

The amino acid sequence of VDAC is highly conserved. The sequence identity/similarity between the human VDAC1, VDAC2 and VDAC3 is 75%/91% and 67%/85% respectively [11]. The high sequence similarity allowed the structural prediction of VDAC2 and VDAC3 by means of homology modeling [4,12]. More recently, the structure of zebrafish VDAC2 was solved at high resolution confirming the same β-barrel arrangement as VDAC1 [11]. The barrel core is basically identical in the three VDAC isoforms that differ only in the N-terminal fragment. In particular, while the N-terminal tail of VDAC1 and VDAC3 only comprises the first 25 residues, the N-terminal fragment of VDAC2 is 11 residues longer and comprises the first 36 residues. The fact that the N-terminal fragment carries a net positive charge suggests its involvement in the channel gating mechanism.

Despite the high sequence homology and the high structural similarity, the three VDAC isoforms appear to be functionally different and, in particular, the behavior of VDAC3 appears to be significantly different from the other two isoforms. For instance, functional experiments demonstrated that recombinant VDAC1 and VDAC2 are able to form pores in lipid bilayers, while recombinant VDAC3 turned out to be poorly active as pore-forming protein either after reconstitution in artificial bilayers or incorporation in liposomes [13]. The functional difference of the VDAC isoforms was also tested through yeast complementation assay, a general method to assess the ability of an externally supplemented protein to recover the physiological growth phenotype in a mutated strain. In particular Δ*porin1* yeast strains were transformed with plasmids expressing the mammalian VDAC isoforms to assess their ability to restore the normal growth phenotype [14]. The experiments showed that VDAC1 and VDAC2 were able to restore the growth phenotype while VDAC3 was not, or it was at a very low level [15]. Interestingly, De Pinto and coworkers showed that replacing the N-terminal domain of VDAC3 with the same domain from VDAC1 fully restored the ability to complement the growth defect in Δ*porin1* yeast [16]. Since the N-terminal tail of VDAC3 and VDAC1 carries the same net charge, this effect is probably not due to a difference in the gating mechanism and may be related to the different number of cysteine residues in the tail instead, two in VDAC3 and none in VDAC1.

The VDAC3 channel is indeed characterized by a peculiar spatial distribution of cysteine residues. When a cysteine residue is exposed on the surface of a protein, it can interact with H-bonding partners (e.g. water molecules). These interactions, polarizing the SH bond, induce a significant decrease of pKa. As a consequence, exposed cysteine residues are the amino acids with the pKa closest to the physiological pH and they can easily shift from the reduced to the oxidized form in response to small fluctuations of the pH. The high reactivity of exposed Cys residues explains why they are found much less frequently than expected on molecular surfaces [17]. It is thus remarkable that in hVDAC3, four out of six cysteine residues (Cys36, Cys65, Cys122, Cys229) are located in loops among the β-strands and are thus exposed to the environment between the inner and outer mitochondrial membranes [18]. Moreover, even if the N-terminal tail is expected to be highly mobile, in the homology model built using the mouse VDAC1 as template, Cys2 also points to the intermembrane space. The exposure of the hVDAC3 cysteines suggests that they should be highly reactive and might play some specific physiological role. For instance, human VDAC2 and VDAC3 with 9 and 6 cysteines, respectively, are more subject to SH oxidation than VDAC1.

In this study we analyzed the impact of potential intramolecular disulfide bonds through Molecular Dynamics (MD) simulations of hVDAC3 derivatives incorporating single disulfide bridges in open channels. As already mentioned, complementation experiments with a VDAC3 chimera where the N-terminal tail was replaced by the corresponding fragment of VDAC1 [16], showed the functional relevance of this region, suggesting a key role for the two cysteine residues located in this flexible domain (Cys2 and Cys8). The high flexibility of the N-tail makes it easy for these two residues to come to a bonding distance. A third potential disulfide bonding partner is represented by Cys122 that (in the homology model) is located very close to Cys2. Very recently, this disulfide bond was proposed to have a critical functional role in VDAC3 [19]. Independently from this reference, we ran MD simulations of derivatives of hVDAC3 incorporating a single disulfide bond in positions 2-8, 2-122 and 8-122 (hereafter referred to as SS-2-8, SS-2-122 and SS-8-122).

In order to study the effect of other possible disulfide bonds, we employed an array of bioinformatics tools to evaluate cysteine oxidation probability and determine the most likely disulfide bond network in hVDAC3. On the basis of the results, we performed the MD simulations of other three derivatives with disulfide bonds in positions 8-65, 2-36 and 8-36 (referred to as SS-8-65, SS-2-36 and SS-8-36). The simulations revealed a drop in conductance from 10% in the case of SS-2-8 up to 50% in SS-8-36. The simulations therefore suggest that, upon external stimuli, the two cysteines of the mobile N-terminal domain can potentially link to different cysteine residues located in the barrel, modulating both the pore size and the electrostatic properties of hVDAC3.

2. Methods

2.1. Molecular dynamics simulations

We have simulated six different variants of the human VDAC3 protein with disulfide bonds in positions 2-8, 2-122, 8-122, 2-36, 8-65 and 8-36. The simulations made use of a homology model of hVDAC3 built using the mouse VDAC1 as template, as detailed in Ref. [12]. Our simulations started from the open configuration of VDAC3 pre-equilibrated for 16 ns in Ref. [12]. The VDAC3 channel was embedded in a bilayer composed by 166 POPE molecules and hydrated with 10,179 water molecules. The system also included 99 chloride and 93 potassium ions so as to enforce electroneutrality and reach a final concentration [KCl] = 0.5 M. After 200 steps of conjugate gradient minimization, the system was gradually heated in the NVT ensemble across the temperature progression 10, 100, 200, 300 K for 50 ps, 1 ns, 5 ns and 10 ns respectively. In all of these equilibration stages a time-step $\delta t = 2$ fs was used to avoid possible steric clashes. In order to enable a speed-up of the calculation, the hydrogen mass was then rescaled by a factor 4.0 which allowed to set a time-step of 4.0 fs.

Using this set-up the system was further equilibrated for 400 ns in the NVT ensemble at 300 °K. Using as input the coordinates of the last frame of this trajectory, but assigning different velocities sampled from the Maxwell–Boltzmann distribution, we then performed 5 independent production runs of 100 ns each in the NVT ensemble. The last frame of three of these runs (randomly chosen) was used as input for simulations in the presence of a membrane potential. Specifically, we ran 3 simulations with a potential of +50 mV and 3 simulations with a potential of −50 mV, not far from the values used in experiments. All simulations were performed with the Amber ff99SBildn [20] force field using the ACEMD [21] molecular dynamics engine.

Since the pioneering studies of Aksimentiev and Schulten [22] the constant electric field approach has become the most widely used method to simulate currents in ion channels. In fact, in order to reduce finite-size effects and avoid modeling interactions with an interface [23], MD simulations are normally run under periodic boundary conditions which imply that the two baths on the two sides of the membranes are actually the same liquid phase which rapidly destroys the concentration gradient initially imposed to drive the ion flow. The most direct strategy to address this problem is to use two parallel bilayers so that the first and third bath constituting a single liquid phase, are effectively separated from the second bath. The downside of this approach is that it dramatically increases the size of the system and thus the computational cost. The constant electric field approach, reviewed in Ref. [24,25] has been shown to be a simple and valid approach for accounting for the membrane potential in MD studies of channel systems.

The versatility of the method was testified by its wide range of applications ranging from the study of ion conduction [26–28] to electroporation [29] and the translocation of DNA and large biomolecules through nanopores [30].

Technically we thus applied a constant external electric field using the in-built plug-in in AceMD, $\Delta V = E * L_z$, where L_z is the dimension of the cell along the z-direction [26]. The contribution to the current provided by an individual ion is computed through the expression:

$$\delta i = \frac{\alpha \delta z}{2\delta t L_Z}.$$

In this expression δz is the displacement of the ion along the channel axis over a period $2\delta t$ corresponding to two trajectory sampling intervals, while L_z is the length of the simulations box in the direction of the channel axis. Using this approach, $\delta z/L_z$ represents the fraction of an electron charge crossing the channel in a time interval $2\delta t$. Finally, $\alpha = 1.6 * 10^{-7}$ is simply a conversion factor to express the current in Ampère. Currents were determined following the time-course of the charge transported across the channel and performing a linear regression of this curve. The error was then estimated as the standard deviation of current and conductance over a number of independent simulations. Indeed, as suggested in Ref. [31], if individual ion crossings are regarded as independent events, the permeation events follow a Poisson distribution and the error on the current in a single trajectory can be computed as $\pm I/\sqrt{N_C}$ where N_C represents the number of crossing events. This error analysis, leading to errors of the same order of magnitude or smaller of the ones yielded by the approach based on the standard deviation, is illustrated in detail in the Supporting Information.

2.2. Bioinformatics analysis

The cysteine oxidation state and the propensity to form disulfide bridges were evaluated using a set of neural networks. The CYSPRED program [32] operates as a standard feed-forward neural network and makes use of evolutionary information through multiple alignments of the sequences where the cysteines are located. CYSPRED can predict cysteine oxidation state but not the disulfide bond partner. The DiANNA (DiAminoacid Neural Network Application) web server [33] uses a three-step procedure. A first neural network is trained to discriminate cysteines in the oxidized and reduced states. This is achieved through the use of both evolutionary and secondary structure information. The user-submitted sequence in fact, is aligned to SWISS-PROT sequences using the PSI-BLAST algorithm and its secondary structure is predicted by the PSIPRED program. After this stage, a second neural network computes a score for each potential disulfide bridge. In the third step of the procedure, the algorithm builds a graph whose nodes are the half-cysteines and whose edges are weighted by the scores computed during the second stage. This complete graph is then pruned through the Edmonds–Gabow maximum weight matching algorithm [34] to identify the sub-graph containing the most probable disulfide bonds.

We used also a third neural network based tool, which is implemented in the DISULFIND web server [35]. Similarly to DiANNA, also DISULFIND identifies, at first, oxidized and reduced cysteines exploiting the secondary structure preference of cysteines and half-cystines and the influence of their flanking sequences. Next, in order to determine the correct disulfide connectivity pattern, the neural network screens the ensemble of graphs $G(V,E)$, where V is the set of half-cystines identified in the previous stage and E is a possible set of edges connecting them. Finally, the predicted connectivity pattern is the one that maximizes a scoring function representing the fraction of correct disulfide bonds in the candidate solution [36]. It is clear that, since the correct set of edges E is not known a priori, the algorithm could not compute the scoring function, in principle. The neural network learns to compute the scoring function during the training phase, when it is presented with all the possible connectivity patterns of the proteins of a training dataset, along with the corresponding scores. All of the algorithms discussed so far make prevalent use of sequence information but disregard the structural features of the protein. The possibility to use structural properties to predict the oxidation state of cysteines is exploited by the COPA (Cysteine Oxidation Prediction Algorithm) algorithm [37]. Physicochemical parameters of oxidation susceptible protein thiols were organized into a database, the Balanced Oxidation Susceptible Cysteine Thiol Database (BALOSCTdb). The analysis of this database with a decision tree classifier led to the identification of three parameters which are critical for prediction of thiol oxidation susceptibility: (1) distance to nearest cysteine sulfur atom, (2) solvent accessibility and (3) the *pKa*. The structure of the decision tree based on these parameters is illustrated in Fig. 1.

3. Results

3.1. MD simulations of VDAC3 with disulfide bonds involving cysteines 2, 8, and 122

The structural features of the disulfide-bond variants of the VDAC3 channel are illustrated in Fig. 2 where we show the last frame of the fifth 100 ns production run. A feature of the wild-type VDAC1 channel is that both the N-terminal and C-terminal tails point towards the mitochondrial intermembrane space [18]. This structural arrangement is conserved when building the VDAC3 by homology modeling using the VDAC1 as template, as showed in Fig. 2, where both the N- and C-terminus point towards the positive z-axis. This feature is clearly retained by the SS-2-122 variant where the 2-122 disulfide bridge moves the N-terminal tail closer to the wall of the barrel. This shift is quantified by the change in the distance between the C_α of residues 2 and 122 from 8.24 Å in the wild-type to 5.0 Å in SS-2-122.

In SS-8-122 the N-terminal tail is also covalently constrained to be in contact with strands 7-8 of the barrel. However, the segment comprising the amino acids 1-7 was free to move and adopted an orientation roughly orthogonal to that of amino acids 8-25, thus crossing the apical part of the channel. The migration of fragment 1-7 appears to be driven by the establishment of a network of hydrogen bonds with a set of polar residues of the barrel: Thr70, Glu88, Asn89, Lys119, and Ser124.

The SS-2-8 variant exhibits a completely different structural motif since the 2-8 disulfide bridge bends the N-tail over itself so that fragment 1-12 now runs downwards and roughly parallel to amino acids 13-25, which are still directed upwards. Despite this marked bend induced by the covalent disulfide bond, the whole N-terminal tail remains closely packed to the wall of the barrel and in particular to the strands 3 to 9.

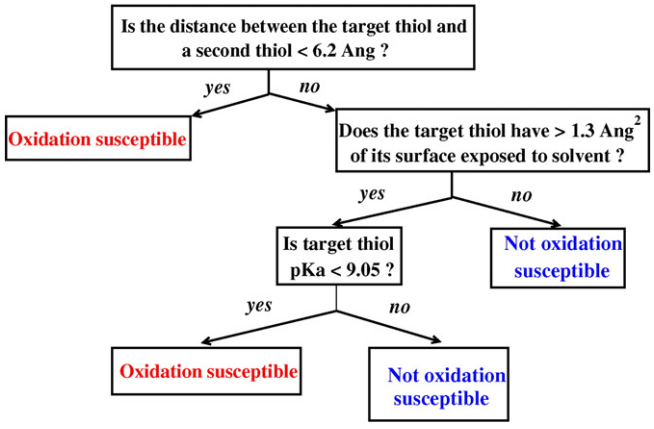

Fig. 1. The optimal decision tree of the COPA algorithm. The tree was identified by the C4.5 classifier run on the BALOSCT database (adapted from Ref. [37]).

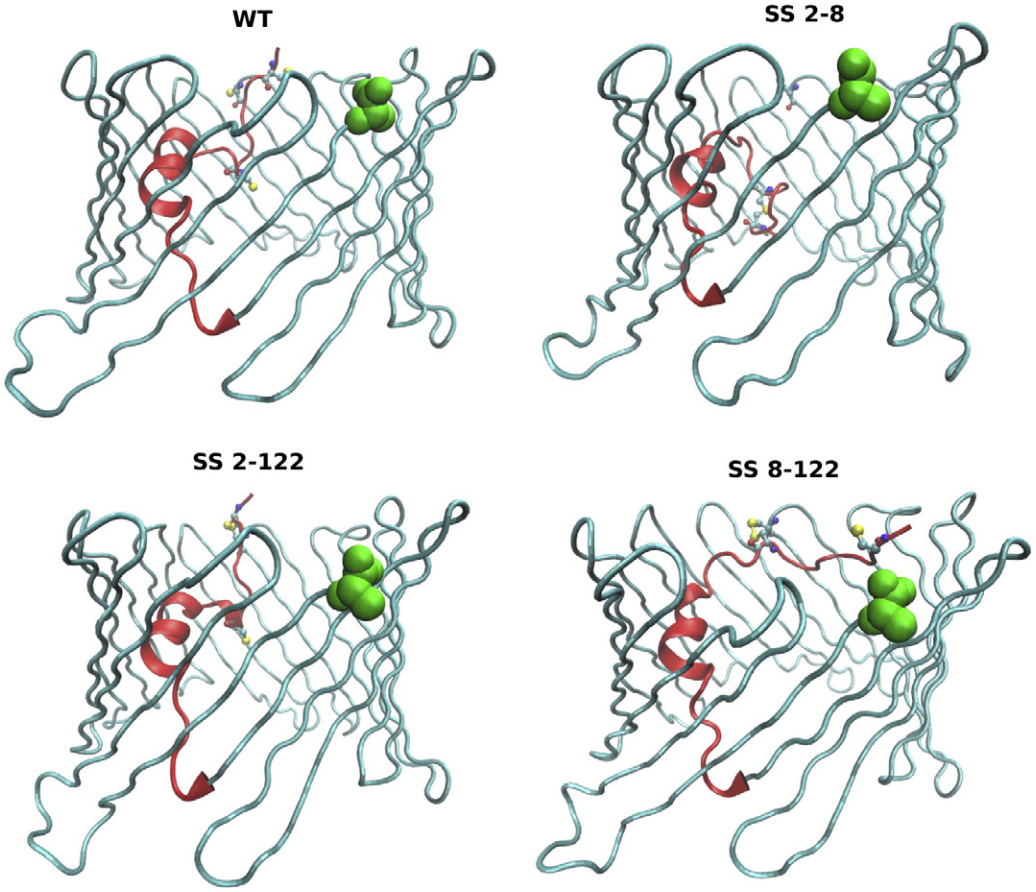

Fig. 2. Typical structures of the Wild-Type VDAC3 channel and of the disulfide-linked variants SS-2-8, SS-2-122, SS-8-122. The N-terminal tail corresponding to fragment 1-25 is shown in red. The C-terminal residue Ala283 is highlighted in green van der Waals representation. The three cysteines involved in the disulfide bonds are shown in a ball-and-stick representation.

The different position of the N-tail results in a different level of obstruction of the channel. This can be better appreciated from Fig. 3 where a top view is shown for the same configurations illustrated in Fig. 2. From Fig. 3 it can be seen that while in the wild-type and in SS-2-8 and SS-2-122 the N-tail is close to one side of the barrel (strands 3-11), in SS-8-122 the N-tail also flanks the strands 12-16 corresponding to 11/19 of the channel profile.

The steric hindrance of the VDAC3 channel determined by the different position of the N-tail in the wild-type and in the disulfide bonded species was quantified through a calculation of the solvent accessible surface area (SASA). The computation was performed using the Shrake–Rupley algorithm [38] as implemented in our in-house program HOPE [39], which compares well with the widely used HOLE program [40].

The profiles of the solvent accessible area are reported in Fig. 4. From this figure, it is clear that in the SS-8-122 species the SASA in the top region of the channel ($5\ \text{Å} < z < 15\ \text{Å}$) is significantly decreased with respect to the wild-type and both SS-2-8 and SS-2-122 forms. A decrease in the SASA also occurs in the lower region of the channel ($-12\ \text{Å} < z < 3\ \text{Å}$) in the case of species SS-2-8 as a result of the downward bend of fragment 1-12 of the N-terminal tail. Assuming the profile of the WT as a reference, it can be noted that the drop in the accessible surface in SS-2-8 is much smaller than that occurring in SS-8-122 (12% vs 46%). This result leads to the expectation that the ion current in SS-8-122 should be significantly lower with respect to the other forms.

The influence on the ionic currents of the different obstruction of the channel in the disulfide-bridged species was estimated by means of simulations in the presence of an electric field. We performed three independent simulations with a transmembrane potential of $+50\ mV$ and three simulations with a potential of $-50\ mV$. The currents and conductivity results are summarized in Table 1 and Fig. 5. First of all, it can be noted that in the absence of a transmembrane potential there cannot be a preferential direction of ion flow so that the average currents are close to zero even if they change significantly from run to run as can be deduced from the large values of the standard deviations. Since the channel is anion selective, the chloride current is dominant with respect to the potassium one and the total current $I_{TOT} = I_K - I_{Cl}$ is positive. The sign of the current is obviously reversed in the presence of a negative potential. Independently of the sign of the potential the ranking of the absolute values of the current in the different species is always $I_{WT} > I_{2\text{-}8} > I_{2\text{-}122} > I_{8\text{-}122}$. These results confirm the impact of the obstruction of the top part of the channel in SS-8-122 and SS-2-122 while the obstruction of the lower part of the channel in SS-2-8 appears to have a minor role. The reduction of the channel cross section also has an impact on the conductance. In particular, the total conductance of SS-8-122 resulted to be decreased by 20% irrespective of the sign of the applied potential. It is also interesting to observe that the drop of the conductance is more pronounced in the case of potassium (decrease of 40%) than chloride (decrease of 20%). Since the van der Waals radius of potassium ($r_K = 1.70$ Å) is smaller than that of chloride ($r_{Cl} = 2.51$ Å) this effect is presumably not related to steric hindrance but rather to a redistribution/shielding of the charges along the channel walls. This is also confirmed by the steric obstruction of the pore, 40% for SS-8-122, compared to a decrease of 20% of the currents.

The comparison of potassium and chloride conductance provides an estimate of channel selectivity. Although all disulfide-bonded species are more anion selective than the wild-type, the anion selectivity of SS-2-122 and SS-8-122 are comparable and smaller than that of SS-2-8. Finally, in agreement with the observations of Rui et al. [41] on the VDAC1 channel, it can be noted that the potassium conductance of all

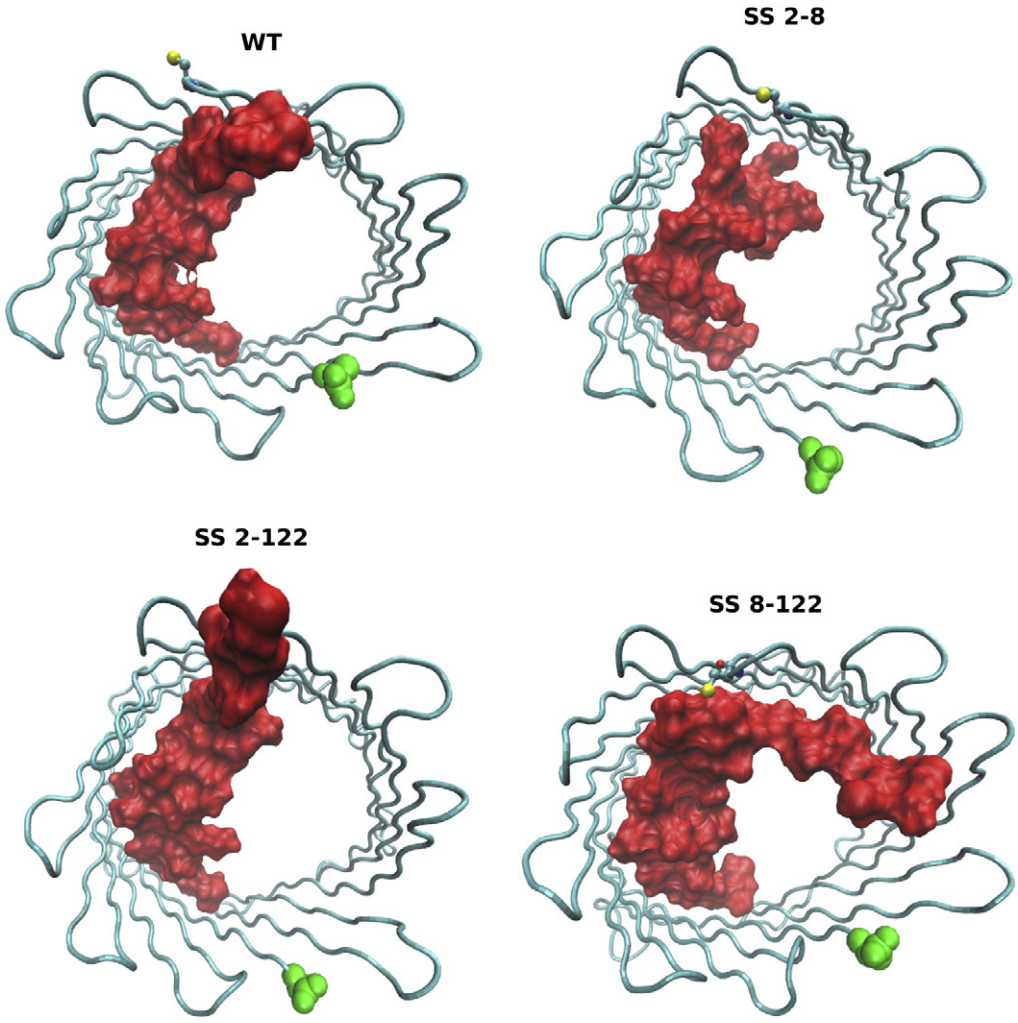

Fig. 3. Top view of the same structures of the wild-type VDAC3 channel and of the disulfide-linked variants SS-2-8, SS-2-122, SS-8-122 also reported in Fig. 2. The N-terminal tail corresponding to fragment 1-25 is shown in red with a surface filling representation that highlights the different degree of obstruction of the channel. The C-terminal residue Ala203 is highlighted in green van der Waals representation. The three cysteines involved in the disulfide bonds are shown in a ball-and-stick representation.

species is larger at negative transmembrane potentials, while chloride conductance is larger at positive potentials. This suggests that also in VDAC3, the potassium ions flow more easily towards the negative direction of the *z*-axis while the situation is reversed in the case of chloride.

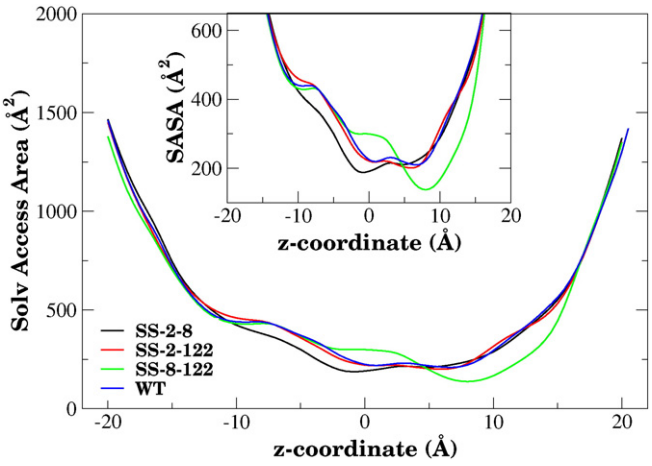

Fig. 4. Profiles of solvent accessible surface area along the axis of the VDAC3 channel. The inset is a zoom of the main graph in the region of the minima of the plots.

3.2. Prediction of hVDAC3 cysteine redox state by bioinformatics analysis

We have analyzed the human VDAC3 protein using different approaches to discriminate the cysteine residues more susceptible to oxidation. When VDAC3 sequence is fed into the DiANNA server [33], only Cys36 is predicted to be potentially prone to an oxidized state. As a consequence, no intra-molecular disulfide bond in VDAC3 is predictable by this procedure. Nevertheless, the DiANNA program assigns a score to all the 15 theoretical disulfide bonds (human VDAC3 contains 6 cysteines). A clear gap can be noted between the score assigned to bond Cys122-Cys229 (~1.0) and the scores of all the other bonds, showing values ranging from 0.01 and 0.02. The second and third largest scores are assigned to Cys8-Cys65 (0.01683) and to Cys65-Cys229 (0.01584) respectively. These scores are used to weight the edges of a complete graph whereby each cysteine is connected with all the others. The most likely disulfide bridges are identified by applying the Edmonds–Gabow maximum weight matching algorithm [34]. After this procedure was applied, the two bonds with the highest score, Cys122-Cys229 and Cys8-Cys65, were still retained. The third most likely disulfide bond is predicted to be Cys2-Cys36.

The DiANNA predictions are in partial agreement with the results of the analysis performed with CYSPRED [32]; DISULFIND [35] predicted all of the cysteines of hVDAC3 to be in the reduced form, so that no intra-molecular disulfide bridges should form. Conversely, CYSPRED suggested the existence of a single cysteine residue capable of forming disulfide

Table 1
Currents and conductances in the hVDAC3 channel and its disulfide bonded derivatives. The data in the absence of the electric fields are averages on five independent runs and are reported to show a current equal to zero, within the experimental error. The data at −50 and +50 are averages on three independent runs. The numbers in brackets indicate the error computed as the standard deviation of individual data.

Species	V (mV)	Itot (pA)	IK (pA)	ICl (pA)	Gtot/G_{WT}	GK (nS)	GCl (nS)
WT	0.0	−11.4 (19.4)	1.4 (8.0)	12.9 (12.7)			
2–8	0.0	−1.1 (18.9)	−10.8 (6.9)	−9.7 (13.1)			
2–122	0.0	2.4 (20.6)	−2.6 (11.2)	−5.1 (26.8)			
8–122	0.0	−0.6 (8.2)	5.5 (7.3)	6.1 (11.3)			
WT	−50	−215.3 (18.8)	−65.1 (13.0)	150.2 (13.9)	1.0	1.3 (0.3)	−3.0 (0.3)
2–8	−50	−198.6 (11.9)	−39.2 (2.8)	159.5 (9.7)	0.9	0.8 (0.1)	−3.2 (0.2)
2–122	−50	−173.7 (11.5)	−44.8 (7.9)	128.9 (6.2)	0.8	0.9 (0.2)	−2.6 (0.1)
8–122	−50	−170.6 (10.6)	−41.3 (5.3)	129.2 (15.8)	0.8	0.8 (0.1)	−2.6 (0.3)
WT	+50	208.8 (16.2)	58.6 (13.2)	−150.1 (20.2)	1.0	1.2 (0.3)	−3.0 (0.4)
2–8	+50	220.8 (26.9)	36.2 (10.4)	−184.5 (16.8)	1.0	0.7 (0.6)	−3.7 (0.3)
2–122	+50	188.5 (47.2)	44.6 (15.4)	−143.9 (34.6)	0.9	0.9 (0.3)	−2.9 (0.7)
8–122	+50	163.2 (9.9)	31.2 (16.9)	−131.9 (6.9)	0.8	0.6 (0.3)	−2.6 (0.1)

bonds, namely Cys2. Overall, the bioinformatics analysis revealed a very low tendency of hVDAC3 to form intra-molecular disulfide bonds.

All of the bioinformatics analyses discussed so far required only the primary sequence of the hVDAC3 protein as input, basically disregarding any structural feature. In order to evaluate the influence of VDAC3 architecture on the oxidation state of the cysteines, we used the final frame of the MD trajectory. Following the COPA algorithm [37], the prediction of thiol oxidation susceptibility was performed considering the distance between the two potentially interacting thiol groups, the solvent accessible area and the *pKa* of the target thiol group. The results of the analysis are reported in Table 2. First of all, it can be noticed that for all cysteines pairs in hVDAC3, the mutual distance is largely exceeding the 6.2 Å cutoff so that no disulfide bond in principle could be formed as an effect of the distance rule. Then, the formation of disulfide bonds in hVDAC3 requires the target thiol to have a solvent accessible area larger than 1.3 $Å^2$ and a pKa lower than 9.05. These criteria are only met by the disulfide bonds including Cys36 as the target thiol. This is because, with the exception of Cys2, all cysteines of hVDAC3 feature a solvent accessible area of the thiol group significantly larger than the 1.3 $Å^2$ cutoff. The discriminating criterion remains the *pKa*. Cys36 shows the lowest *pKa* among the cysteines of hVDAC3 and, in particular, it is the only one whose *pKa* is below the 9.05 cutoff. The special role predicted by the COPA algorithm for Cys36 thus appears to be consistent with the DiANNA prediction according to which Cys36 was the only cysteine capable of forming disulfide bonds. The role of *pKa* also explains the oxidized state that CYSPRED predicts for Cys2 since this residue features the third lowest pKa among all the hVDAC3 cysteines.

Another feature known to lower the *pKa* of cysteine residues is the presence of basic amino acids in close proximity. The influence of basic residues on hVDAC3 cysteines was assessed by computing the fraction of frames in the 1 μs NVT trajectory in which each cysteine was in contact with a basic residue. The calculation was repeated using 5.0 Å and 3.0 Å distance cutoff. The probability of interaction with basic residues is rather small (for a few cysteines) with the largest cutoff and drops to zero for all cysteines when considering the more realistic lowest cutoff. This suggests that the reactivity of hVDAC3 cysteines depends more on their surface exposure than on the presence of basic residues in their neighborhood.

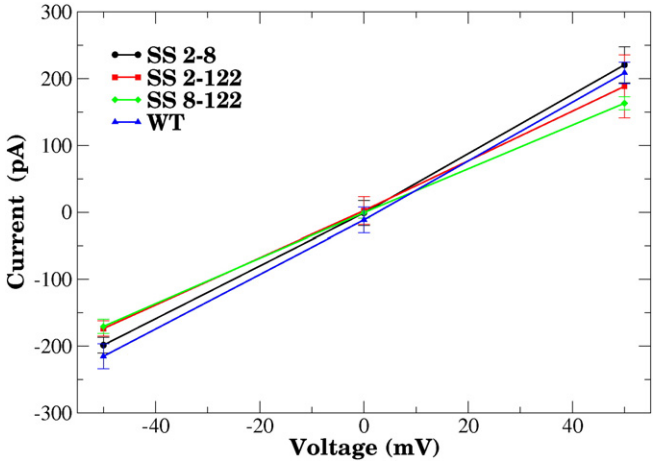

Fig. 5. Current–voltage relationship for the VDAC3 channel: comparison of wild-type and disulfide bridged derivatives.

3.3. MD simulations of VDAC3 containing disulfide bonds 2-36, 8-36, and 8-65

In order to select a second set of likely disulfide bonds, the prediction by bioinformatics tools must be filtered using the constraints posed by the 3D-structure of the protein. According to the DiANNA neural

Table 2
Cysteine oxidation prediction using the COPA algorithm. Columns 1 and 2 report respectively the target cysteine and the potential partner in a disulfide bond; column 3 shows the distance between the S_γ atoms of the two cysteins; column 4 lists the solvent accessible area; column 5 reports the pKa of the target thiol; and column 6 contains the prediction of the oxidation state of the target thiol.

Target Cys	2nd-Cys	Dist Å	SASAtarg $Å^2$	pKatarg	OXYtarg
2	8	16.67	0.806	9.26	RED
2	36	30.63	0.806	9.26	RED
2	65	16.93	0.806	9.26	RED
2	122	11.25	0.806	9.26	RED
2	229	32.56	0.806	9.26	RED
8	2	16.67	55.906	9.52	RED
8	36	34.63	55.906	9.52	RED
8	65	25.57	55.906	9.52	RED
8	122	19.27	55.906	9.52	RED
8	229	32.56	55.906	9.52	RED
36	2	30.63	71.650	8.09	OXY
36	8	34.63	71.650	8.09	OXY
36	65	15.89	71.650	8.09	OXY
36	122	39.74	71.650	8.09	OXY
36	229	28.59	71.650	8.09	OXY
65	2	16.93	47.901	9.15	RED
65	8	25.57	47.901	9.15	RED
65	36	15.89	47.901	9.15	RED
65	122	27.61	47.901	9.15	RED
65	229	32.21	47.901	9.15	RED
122	2	11.25	51.280	9.40	RED
122	8	19.27	51.280	9.40	RED
122	36	39.74	51.280	9.40	RED
122	65	27.61	51.280	9.40	RED
122	229	33.50	51.280	9.40	RED
229	2	32.56	40.851	9.33	RED
229	8	32.56	40.851	9.33	RED
229	36	28.59	40.851	9.33	RED
229	65	32.21	40.851	9.33	RED
229	122	33.50	40.851	9.33	RED

network, the most probable disulfide links are Cys2-Cys36, Cys8-Cys65 and Cys122-Cys229. The first two bonds could be established exploiting the high mobility of the N-terminal tail of hVDAC3. The third bond, however, should connect two cysteines located at the tips of two β-hairpins of the barrel, which are very distant from each other (hairpins 7-8 and 15-16).

It must be stressed, however, that even if some cysteine residues are unlikely to form intramolecular disulfide bonds, they may be involved in intermolecular SS-bridges. In this way they may stabilize dimers such as those recently discovered in zebrafish VDAC2 [11]. Other potential intramolecular disulfide bonds are those involving Cys36 due to its very low *pKa* as highlighted above. Of these bonds, however, Cys36-Cys122 and Cys36-Cys229 present the same problem as Cys122-Cys229, requiring the connection of very distant cysteines. Conversely, bond Cys36-Cys65 could link two cysteines on the tip of two neighboring hairpins (1-2 and 3-4). However, such a bond is unlikely to significantly occlude the channel and able to reduce the conductance. Thus, it was not of interest and was excluded from the present study. Finally, the only remaining disulfide bond involving Cys36 is the one exploiting the mobility of the N-terminal tail, Cys8-Cys36. As a consequence, in theory, disulfide bonds potentially capable of reducing the permeability of the pore are Cys2-Cys36, Cys8-Cys65 and Cys8-Cys36.

The derivatives of hVDAC3 including these bridges were simulated using the same protocol employed above. The comparison of the profiles of the solvent accessible area (Fig. 6) shows that the ability of SS-8-65 to obstruct the channel is roughly the same as that of SS-8-122 for $z > 11$ Å, but in the central part of the channel the solvent accessible area of SS-8-65 is higher than that of SS-8-122. This behavior can be understood by analyzing the final structures (Figs. 7 and 8) of the simulations in the absence of electric field. As already discussed, in SS-8-122 the N-terminal tail is constrained to be in contact with the β-strands 7-8, leaving enough space for the fragment 1-7 to adopt a conformation orthogonal to that of fragment 8-25 and thus crossing the apical part of the channel and obstructing it. Conversely, in SS-8-65 the N-tail is covalently linked to strands 3-4 so that there is not enough space for amino acids 1-7 to cross the channel: rather the fragment 1-7 can move along the axial direction towards the upper opening.

An interesting structural behavior is also exhibited by SS-2-36 and SS-8-36. The disulfide bond involves Cys36 with different partners. Cys2 is located at the very beginning of the N-terminal tail. As a result, in SS-2-36, the fragment 1-11 is roughly orthogonal to helix 12-20 and is stretched along the profile of the barrel wall in correspondence of strands 3 to 11. On the other hand, in the species SS-8-36, the location of Cys8 determines the stretching of fragment 8-14, which occupies the central part of the barrel cavity, while fragment 1-7 folds back and flanks the barrel wall in correspondence of strands 3 to 8. As can be better appreciated from the top view (Fig. 8), the N-terminal tail adopts a sort of twisted S-like shape that leads to a larger obstruction of the top part of the channel. This is confirmed by the profiles of the accessible area showing that for $z > 7.5$ Å the SASA of SS-8-36 is smaller than that of SS-8-122, which on turn is smaller than that of SS-2-36. Conversely, for $z < 7.5$ Å, the SASA profile of SS-8-36 is practically identical to that of SS-8-122, while the SASA of SS-2-36 is significantly smaller than that of the other two species. This is presumably due to the fact that in SS-8-122 and SS-8-36, the involvement of an internal residue of segment 1-25 in the disulfide bond, lifts the whole N-tail upwards, reducing the level of occlusion of the central region of the channel and increasing the occlusion of the upper part. The different level of obstruction of the channel in the different disulfide-bonded derivatives was reflected in the values of current and conductance. As reported in Table 3 and Fig. 9, both at −50 and +50 *mV* the absolute values of the current and of the conductance of SS-8-36 are much smaller than the corresponding values in SS-2-36 and SS-8-65. The relationship between currents and conductances of SS-2-36 and SS-8-65 depends on the sign of the applied voltage and on the charge of the permeant ions. At −50 *mV* current and conductance of both potassium and chloride ions in SS-2-36 are lower than their counterparts in SS-8-65. However, at +50 *mV* current and conductance of potassium ions in SS-2-36 are lower than the corresponding values in SS-8-65 while the opposite holds for chloride ions. Similar to what was observed in the first set of simulations, potassium conductance drop (by 60%–70% at negative potentials and by 45%–70% at positive potentials) is much more pronounced than the decrease of chloride conductance (by 10%–30% at −50 *mV* and by 20%–40% at +50 *mV*). Also in this case, this is likely to be the effect of a change of the charge distribution inside the channel.

The total current and conductance in these three species are smaller than the corresponding values in SS-8-122 (the most occluded species identified in the first set of simulations). In particular, it can be noted that the total conductance of SS-8-36 drops by 45% (at −50 mV) and 40% (at +50 mV) with respect to the conductance of the species without disulfide bonds. The conductance drop of species SS-2-36 and SS-8-65 is more contained but still significant. The total conductance of SS-2-36 decreases by 30% at both potentials, while the conductance of SS-8-65 exhibits a decrease by 25% and 30% at −50 and +50 mV, respectively.

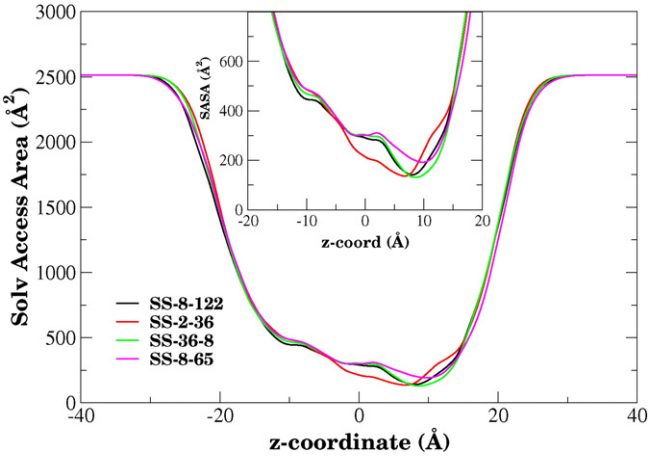

Fig. 6. Profiles of solvent accessible surface area along the axis of the VDAC3 channel. The figure compares the SASA profiles of species SS-8-65, SS-2-36 and SS-8-36 to that of compound SS-8-122 that was characterized by the greatest channel occlusion in the first group of simulations. The inset is a zoom of the main graph in the region of the minima of the plots.

4. Discussion and conclusions

Despite the high sequence homology and structural similarity of the human VDAC isoforms, the mode of action and physiological role of VDAC3 is still highly elusive. An intriguing feature of VDAC3 that might explain the differences with the best known VDAC1 is the higher number of cysteines located on the protein surface protruding towards the mitochondrial inter-membrane space.

In this study we tested the impact of disulfide bridges by means of MD simulations of different hVDAC3 derivatives. We obtained a modulation of the current up to 50% of the total current in the absence of any disulfide bridge. The first set of investigated disulfide bonds was identified through direct inspection of the hVDAC3 channel structure and considering yeast complementation experiments on a VDAC3 chimera [16], namely SS-2-8, SS-2-122 and SS-8-122. In SS-2-8 the N-terminal tail folds back upon itself partially occluding the lower part of the channel. A more significant obstruction of the channel, leading to a conductance drop of 20%, was attained by SS-8-122 where amino acid sequence 1-7 of the N-tail crosses the top part of the channel.

In order to realize a more systematic exploration of the potential disulfide bonds, we identified the most likely SS-bonds using neural networks and structural bioinformatics approaches. Considering the results of the bioinformatics analysis and accounting for the constraints

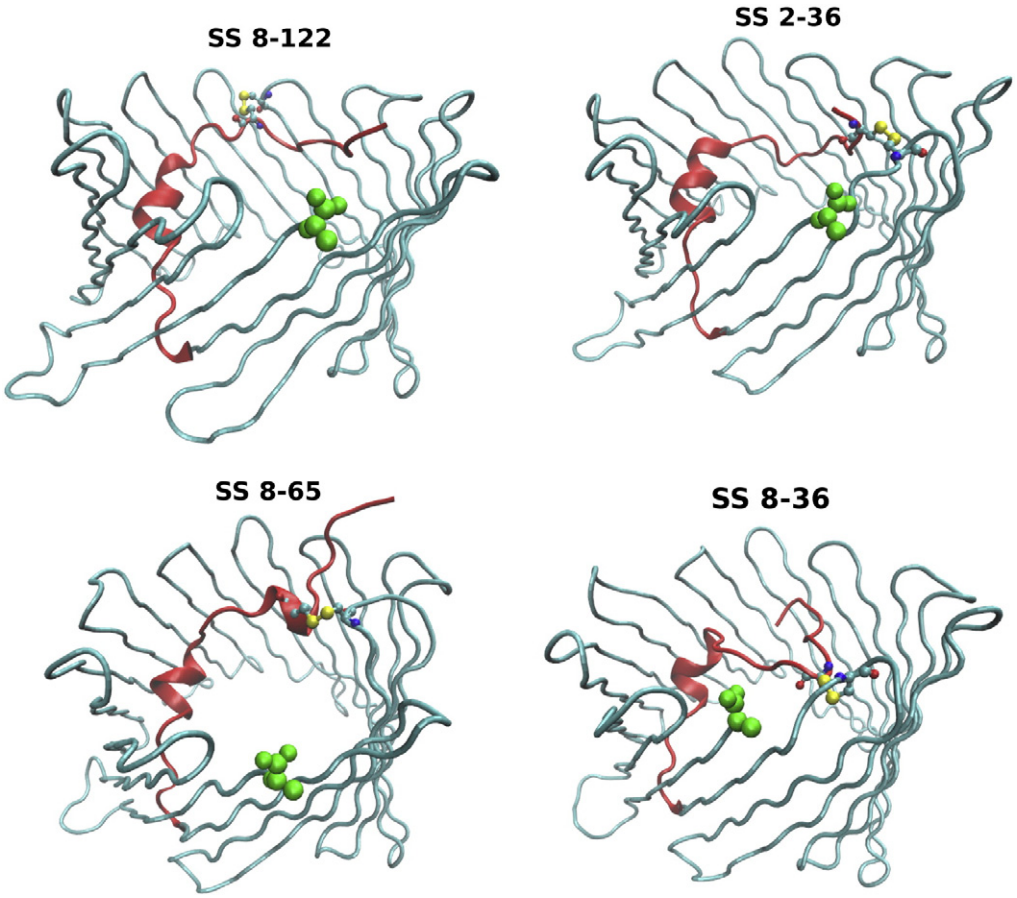

Fig. 7. Typical structures of the disulfide-linked variants SS-8-65, SS-2-36, SS-8-36 and SS-8-122. The N-terminal tail corresponding to fragment 1-25 is shown in red. The C-terminal residue Ala283 is highlighted in green van der Waals representation. The cysteines involved in the disulfide bond are shown in a ball-and-stick representation.

imposed by the tertiary structure of the channel, we identified the most probable disulfide bonds as Cys2-Cys36, Cys8-Cys36 and Cys8-Cys65. The placement of the disulfide bond in position 2-36 or 8-65 turned out to determine a conductance decrease of about 30%. A more efficient closure of the channel was observed in SS-8-36, where the fragment 8-14 blocks the central part of the cavity while amino acids 1-7 fold back running anti-parallel to 8-14 and flank the barrel wall in correspondence of strands 3-8. In this arrangement the sequence 8-14 blocks the central part of the lumen while segment 1-7 occludes the peripheral region. This leads to a conductance decrease of more than 40%, depending on the sign of the applied voltage.

An interesting benchmark for our study is represented by a recent work by Okazaki et al. [19] where it was shown that the recombinant human VDAC3, refolded into planar lipid bilayers, has a weak gating that, upon addition of reducing dithiothreitol or S-nitrosoglutathione, resulted in a normalized conductance profile $g(V)/g_{max}$ comparable to that exhibited by VDAC1. Moreover, site directed mutagenesis experiments showed that the VDAC1-like conductance state could be restored through the C122A and C2A/C8A mutations. These results would suggest that the voltage-dependent gating of VDAC3 can be blocked by disulfide bonds established by Cys122 with either Cys2 or Cys8. This result is in agreement with our simulations showing that the Cys8-Cys122 bond can significantly occlude the upper part of the channel causing a 20% decrease of the conductance and with a lower extent also Cys2-Cys122.

It is remarkable that the disulfide bond proposed as responsible for the pore partial closure is not included among the most likely ones predicted by the DiANNA neural network and the COPA algorithm. These discrepancies suggest the opportunity to reconsider the features that a disulfide bond should have to be an effective channel blocker. These key features are: (i) the likelihood of the disulfide bond; (ii) the ability of the disulfide bond to occlude the channel when it is in the open conformation; and (iii) the ability of the disulfide bond to stabilize the closed conformation. As already discussed, the likelihood of a disulfide bond can be assessed through neural networks or structural bioinformatics tools, while the ability of the disulfide bond to occlude the open state of a channel can be evaluated through MD simulations.

Even if caution must be exercised in evaluating the results obtained with a homology modeling, our simulations show that disulfide bonds can significantly occlude the open state of the VDAC3 channel, reducing the current of both ionic species. This feature sets VDAC3 apart from the other members of the VDAC family. VDAC1, in fact, contains two cysteines, one exposed to the lipid bilayer (Cys127) and one facing the pore cavity (Cys232). The two cysteines are located on strands 8 and 16 respectively, occupying diametrally opposite positions in the barrel, so that a disulfide bond between them is extremely unlikely. Not surprisingly then, the bilayer-reconstituted channel activity of C127A/C232A-rVDAC1 was found to be similar to that of native rVDAC1, with respect to conductance and voltage-dependence, suggesting that VDAC1 cysteines have no influence on the transport of ions, nucleotides and other metabolites [42]. The same study showed that VDAC1 cysteines are not involved in ROS-induced apoptosis that could be induced by hydroxyl radicals generating compounds like H_2O_2 even in cysteine-less rVDAC1.

Human VDAC2 contains 9 cysteines two of which, Cys8 and Cys13, located on the N-terminal tail and other five sitting on the loops of the barrel, in positions similar to the cysteines of hVDAC3. When the VDAC2 wild type was compared with the cysteine-less mutant, it was observed that cysteine residues are involved in anchoring the barrel to its lipid environment [43,44]. The cysteine-less mutant appears to be more structured with respect to the wild type, but this structural

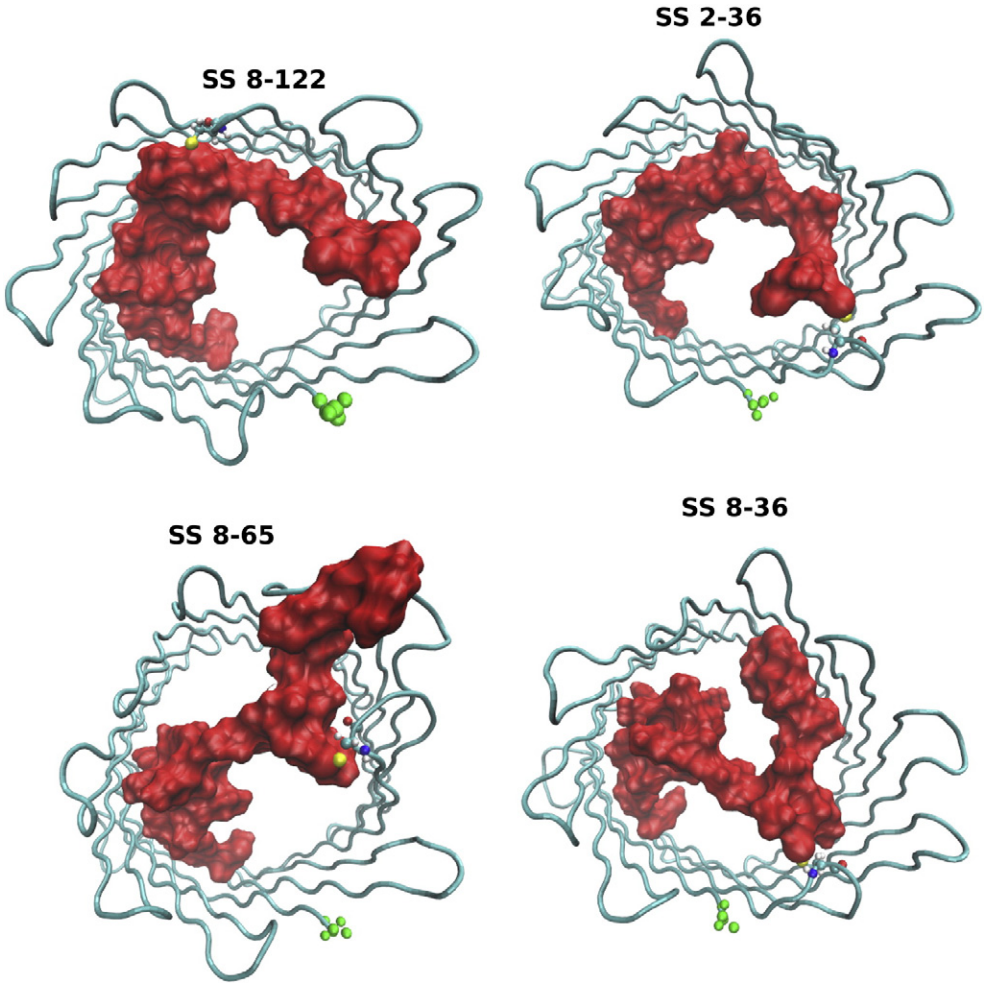

Fig. 8. Top view of the same structures of the disulfide-linked variants SS-8-65, SS-2-36, SS-8-36 and SS-8-122 also reported in Fig. 7. The N-terminal tail corresponding to fragment 1-25 is shown in red with a surface filling representation that highlights the different degree of obstruction of the channel. The C-terminal residue Ala283 is highlighted in green van der Waals representation. The cysteines involved in the disulfide bond are shown in a ball-and-stick representation.

stabilization comes at the expense of the loss of strong protein-lipid interactions.

The human VDAC3 was shown to have channel activity with a very small conductance with respect to hVDAC1 [15]. Disulfide bonds were traditionally believed to play essentially a structural role, reducing the entropy of the unfolded state and stabilizing the native state, which is particularly useful in the case of proteins functioning in a fluctuating cellular environment. However, it now appears [45], that reversible disulfide bond cleavage and formation might have a regulatory role. Many redox regulated proteins function in the first line of oxidative stress defense, acting as transcriptional regulators (e.g. OxyR, Yap1p), which rapidly induce the expression of antioxidant genes to detoxify ROS and repair the damage; chaperones (e.g. Hsp33), which prevent oxidative stress-induced protein aggregation; or metabolic enzymes (e.g. glyceraldehyde-3-phosphate dehydrogenase) that re-route metabolism to increase the production of reducing power increasing the cell's capacity to defend against oxidative stress. The redox modification of disulfide bonds can also affect the structure and function of ion regulatory

Table 3
Currents and conductances in the wild-type and in the disulfide bonded derivatives SS-2-36, SS-8-65 and SS-8-36 of the VDAC3 channel. The data in the absence of the electric fields are averages on five independent runs and are reported to show a current equal to zero, within the experimental error. The data at −50 and +50 mV are averages on three independent runs. The numbers in brackets indicate the errors computed as the standard deviation of individual data.

Species	V (mV)	Itot (pA)	IK (pA)	ICl (pA)	G_{TOT}/G_{WT}	GK (nS)	GCl (nS)
WT	0.0	−11.4 (19.4)	1.4 (8.0)	12.9 (12.7)	-		
2–36	0.0	6.8 (11.2)	−3.2 (11.1)	−5.4 (9.7)	-		
8–65	0.0	3.9 (2.6)	−6.4 (7.3)	−9.0 (9.4)	-		
8–36	0.0	10.3 (13.4)	−4.2 (7.3)	−14.4 (13.5)	-		
WT	−50	−215.3 (18.8)	−65.1 (13.0)	150.2 (13.9)	1.0	1.3 (0.3)	−3.0 (0.3)
2–36	−50	−145.9 (16.2)	−25.6 (8.3)	120.3 (22.3)	0.7	0.5 (0.1)	−2.4 (0.4)
8–65	−50	−159.4 (16.8)	−25.7 (8.2)	133.7 (10.0)	0.75	0.5 (0.4)	−2.7 (0.2)
8–36	−50	−124.8 (26.5)	−20.0 (12.7)	104.8 (14.6)	0.6	0.4 (0.2)	−2.1 (0.3)
WT	+50	208.8 (16.2)	58.6 (13.2)	−150.1 (20.2)	1.0	1.2 (0.3)	−3.0 (0.4)
2–36	+50	146.4 (37.0)	25.1 (2.6)	−121.3 (37.1)	0.7	0.5 (0.1)	−2.4 (0.7)
8–65	+50	144.7 (16.3)	32.3 (9.6)	−112.4 (21.2)	0.7	0.6 (0.2)	−2.2 (0.4)
8–36	+50	115.0 (26.8)	22.5 (5.5)	−92.5 (31.3)	0.55	0.4 (0.1)	−1.8 (0.6)

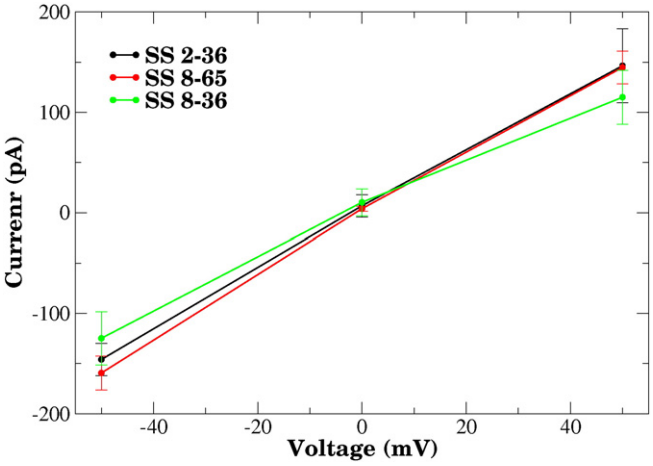

Fig. 9. Current–voltage relationship for the VDAC3 channel: comparison of the disulfide bridged derivatives of hVDAC3 SS-2-36, SS-8-65 and SS-8-36.

proteins including ion channels, pumps and transporters [46]. The electrophysiological activity of VDAC3 might also be regulated by redox signals that induce disulfide bond formation, activating an apoptotic pathway. This hypothesis appears to be consistent with Δ*porin1* yeast complementation experiments [16]. The yeast depleted of the endogenous porin appeared to be very sensitive to ROS. When the yeast was transformed with human VDACs, it was observed that the VDAC3-transformed yeast was constantly the least resistant, while VDAC2 the most. The role of VDAC3 as a sensor of the redox state is also suggested by the particular location of the cysteine residues. VDAC3 interacts with several proteins and this can also be an important issue about the role of its cysteines [47]. The particular placement of the cysteine residues in VDAC3 therefore makes this molecule particularly suitable to waylay the diffusing ROS.

Overall, our results show that the establishment of disulfide bonds in VDAC3 can occlude the channel modulating pore size and current/conductance. This may be the signature of a protein whose activity is dependent on the redox state of its cysteine residues. By analogy to the behavior of other proteins liable to the reversible formation/dissolution of disulfide bonds [48,49], it may be speculated that this mechanism is part of a defense strategy against oxidative stress. Further research efforts will be required to confirm or disprove this scenario, clarifying the role of the VDAC3 channel.

Transparency document

The Transparency document associated with this article can be found, in online version.

Acknowledgment

The authors gratefully acknowledge financial support from the MIUR (PRIN 2010CSJX4F).

References

[1] R. Benz, Permeation of hydrophilic solutes through mitochondrial outer membranes: review on mitochondrial porins, Biochim. Biophys. Acta 1197 (1994) 167–196.
[2] M. Colombini, VDAC: the channel at the interface between mitochondria and the cytosol, Mol. Cell. Biochem. 256-257 (2004) 107–115.
[3] V. Shoshan-Barmatz, V. De Pinto, M. Zweckstetter, Z. Raviv, N. Keinan, N. Arbel, VDAC, a multi-functional mitochondrial protein regulating cell life and death, Mol. Asp. Med. 31 (2010) 227–285, http://dx.doi.org/10.1016/j.mam.2010.03.002.
[4] A. Messina, S. Reina, F. Guarino, V. De Pinto, VDAC isoforms in mammals, Biochim. Biophys. Acta 1818 (6) (2012) 1466–1476.
[5] M.J. Young, D.C. Bay, G. Hausner, D.A. Court, The evolutionary history of mitochondrial porins, BMC Evol. Biol. 7 (2007) 31, http://dx.doi.org/10.1186/1471-2148-7-31.
[6] S. Hiller, R.G. Garces, T.J. Malia, V.Y. Orekhov, M. Colombini, G. Wagner, Solution structure of the integral human membrane protein VDAC-1 in detergent micelles, Science 321 (2008) 1206–1210, http://dx.doi.org/10.1126/science.1161302.
[7] M. Bayrhuber, T. Meins, M. Habeck, S. Becker, K. Giller, S. Villinger, et al., Structure of the Human Voltage-Dependent Anion Channel, Proceedings of the …, 2008.
[8] R. Ujwal, D. Cascio, J.-P. Colletier, S. Faham, J. Zhang, L. Toro, et al., The crystal structure of mouse VDAC1 at 2.3 Å resolution reveals mechanistic insights into metabolite gating, Proceedings of the…, 2008.
[9] A. Kumar, E. Hajjar, P. Ruggerone, M. Ceccarelli, Structural and dynamical properties of the porins OmpF and OmpC: insights from molecular simulations, J. Phys. Condens. Matter 22 (2010) 454125, http://dx.doi.org/10.1088/0953-8984/22/45/454125.
[10] M. Colombini, ScienceDirect.com - Biochimica et Biophysica Acta (BBA) - Biomembranes - VDAC structure, selectivity, and dynamics, Biochim. Biophys. Acta Biomembr. 1818 (6) (2012) 1457–1465.
[11] J. Schredelseker, A. Paz, C.J. Lopez, C. Altenbach, C.S. Leung, M.K. Drexler, et al., High resolution structure and double electron–electron resonance of the zebrafish voltage-dependent anion channel 2 reveal an oligomeric population, J. Biol. Chem. 289 (2014) 12566–12577, http://dx.doi.org/10.1074/jbc.M113.497438.
[12] G.F. Amodeo, M.A. Scorciapino, A. Messina, V. De Pinto, M. Ceccarelli, Charged residues distribution modulates selectivity of the open state of human isoforms of the voltage dependent anion-selective channel, PLoS ONE 9 (2014), e103879, http://dx.doi.org/10.1371/journal.pone.0103879.
[13] X. Xu, W. Decker, M.J. Sampson, W.J. Craigen, M. Colombini, Mouse VDAC isoforms expressed in yeast: channel properties and their roles in mitochondrial outer membrane permeability, J. Membr. Biol. 170 (1999) 89–102.
[14] E. Blachly-Dyson, E.B. Zambronicz, W.H. Yu, V. Adams, E.R. McCabe, J. Adelman, et al., Cloning and functional expression in yeast of two human isoforms of the outer mitochondrial membrane channel, the voltage-dependent anion channel, J. Biol. Chem. 268 (1993) 1835–1841.
[15] V. Checchetto, S. Reina, A. Magrì, I. Szabo, V. De Pinto, Recombinant human voltage dependent anion selective channel isoform 3 (hVDAC3) forms pores with a very small conductance, Cell. Physiol. Biochem. 34 (2014) 842–853, http://dx.doi.org/10.1159/000363047.
[16] S. Reina, V. Palermo, A. Guarnera, F. Guarino, A. Messina, C. Mazzoni, et al., Swapping of the N-terminus of VDAC1 with VDAC3 restores full activity of the channel and confers anti-aging features to the cell, FEBS Lett. 584 (2010) 2837–2844, http://dx.doi.org/10.1016/j.febslet.2010.04.066.
[17] S.M. Marino, V.N. Gladyshev, Analysis and functional prediction of reactive cysteine residues, J. Biol. Chem. 287 (2012) 4419–4425, http://dx.doi.org/10.1074/jbc.R111.275578.
[18] M.F. Tomasello, F. Guarino, S. Reina, A. Messina, V. De Pinto, The voltage-dependent anion selective channel 1 (VDAC1) topography in the mitochondrial outer membrane as detected in intact cell, PLoS ONE 8 (2013), e81522, http://dx.doi.org/10.1371/journal.pone.0081522.
[19] M. Okazaki, K. Kurabayashi, M. Asanuma, Y. Saito, K. Dodo, M. Sodeoka, VDAC3 gating is activated by suppression of disulfide-bond formation between the N-terminal region and the bottom of the pore, Biochim. Biophys. Acta 1848 (2015) 3188–3196, http://dx.doi.org/10.1016/j.bbamem.2015.09.017.
[20] K. Lindorff-Larsen, S. Piana, K. Palmo, P. Maragakis, J.L. Klepeis, R.O. Dror, et al., Improved side-chain torsion potentials for the Amber ff99SB protein force field, Proteins 78 (2010) 1950–1958, http://dx.doi.org/10.1002/prot.22711.
[21] M.J. Harvey, G. Giupponi, G. De Fabritiis, ACEMD: accelerating biomolecular dynamics in the microsecond time scale, J. Chem. Theory Comput. 5 (2009) 1632–1639, http://dx.doi.org/10.1021/ct9000685.
[22] A. Aksimentiev, K. Schulten, Imaging alpha-hemolysin with molecular dynamics: ionic conductance, osmotic permeability, and the electrostatic potential map, Biophys. J. 88 (2005) 3745–3761, http://dx.doi.org/10.1529/biophysj.104.058727.
[23] G. Petraglio, M. Ceccarelli, M. Parrinello, Nonperiodic boundary conditions for solvated systems, J. Chem. Phys. 123 (2005) 044103, http://dx.doi.org/10.1063/1.1955449.
[24] J. Gumbart, F. Khalili-Araghi, M. Sotomayor, B. Roux, Constant electric field simulations of the membrane potential illustrated with simple systems, Biochim. Biophys. Acta 1818 (2012) 294–302, http://dx.doi.org/10.1016/j.bbamem.2011.09.030.
[25] N. Modi, M. Winterhalter, U. Kleinekathöfer, Computational modeling of ion transport through nanopores, Nanoscale 4 (2012) 6166–6180, http://dx.doi.org/10.1039/C2NR31024D.
[26] S. Pezeshki, C. Chimerel, A.N. Bessonov, M. Winterhalter, U. Kleinekathöfer, Understanding ion conductance on a molecular level: an all-atom modeling of the bacterial porin OmpF, Biophys. J. 97 (2009) 1898–1906, http://dx.doi.org/10.1016/j.bpj.2009.07.018.
[27] C. Maffeo, A. Aksimentiev, Structure, dynamics, and ion conductance of the phospholamban pentamer, Biophys. J. 96 (2009) 4853–4865, http://dx.doi.org/10.1016/j.bpj.2009.03.053.
[28] M.Ø. Jensen, D.W. Borhani, K. Lindorff-Larsen, P. Maragakis, V. Jogini, M.P. Eastwood, et al., Principles of conduction and hydrophobic gating in K^+ channels, Proc. Natl. Acad. Sci. 107 (2010) 5833–5838, http://dx.doi.org/10.1073/pnas.0911691107.
[29] R.A. Böckmann, B.L. de Groot, S. Kakorin, E. Neumann, H. Grubmüller, Kinetics, statistics, and energetics of lipid membrane electroporation studied by molecular dynamics simulations, Biophys. J. 95 (2008) 1837–1850, http://dx.doi.org/10.1529/biophysj.108.129437.
[30] A. Aksimentiev, Deciphering ionic current signatures of DNA transport through a nanopore, Nanoscale 2 (2010) 468–483, http://dx.doi.org/10.1039/b9nr00275h.
[31] M. Sotomayor, V. Vásquez, E. Perozo, K. Schulten, Ion conduction through MscS as determined by electrophysiology and simulation, Biophys. J. 92 (2007) 886–902, http://dx.doi.org/10.1529/biophysj.106.095232.

[32] P. Fariselli, P. Riccobelli, R. Casadio, Role of evolutionary information in predicting the disulfide-bonding state of cysteine in proteins, Proteins: Struct., Funct., Bioinf. 36 (1999) 340–346, http://dx.doi.org/10.1002/(SICI)1097-0134(19990815)36:3<340::AID-PROT8>3.0.CO;2-D.
[33] F. Ferrè, P. Clote, DiANNA: a web server for disulfide connectivity prediction, Nucleic Acids Res. 33 (2005) W230–W232, http://dx.doi.org/10.1093/nar/gki412.
[34] L. Lovász, M.D. Plummer, Matching Theory, Akadémiai Kiadó, Budapest, Also North-Holland Mathematics Studies, vol. 121, 1986 1986.
[35] A. Ceroni, A. Passerini, A. Vullo, P. Frasconi, DISULFIND: a disulfide bonding state and cysteine connectivity prediction server, Nucleic Acids Res. 34 (2006) W177–W181, http://dx.doi.org/10.1093/nar/gkl266.
[36] A. Vullo, P. Frasconi, Disulfide connectivity prediction using recursive neural networks and evolutionary information, Bioinformatics 20 (2004) 653–659, http://dx.doi.org/10.1093/bioinformatics/btg463.
[37] R. Sanchez, M. Riddle, J. Woo, J. Momand, Prediction of reversibly oxidized protein cysteine thiols using protein structure properties, Protein Sci. 17 (2008) 473–481, http://dx.doi.org/10.1110/ps.073252408.
[38] A. Shrake, J.A. Rupley, Environment and exposure to solvent of protein atoms. Lysozyme and insulin, J. Mol. Biol. 79 (1973) 351–371.
[39] K.R. Mahendran, E. Hajjar, T. Mach, M. Lovelle, A. Kumar, I. Sousa, et al., Molecular basis of enrofloxacin translocation through OmpF, an outer membrane channel of *Escherichia coli* — when binding does not imply translocation, J. Phys. Chem. B Condens. Matter Mater. Surf. Interfaces & Biophys. 114 (2010) 5170–5179, http://dx.doi.org/10.1021/jp911485k.
[40] O.S. Smart, J.G. Neduvelil, X. Wang, B.A. Wallace, M.S. Sansom, HOLE: a program for the analysis of the pore dimensions of ion channel structural models, J. Mol. Graph. 14 (1996) 354–60– 376.
[41] H. Rui, K.I. Lee, R.W. Pastor, W. Im, Molecular dynamics studies of ion permeation in VDAC, Biophys. J. 100 (2011) 602–610, http://dx.doi.org/10.1016/j.bpj.2010.12.3711.
[42] L. Aram, S. Geula, N. Arbel, V. Shoshan-Barmatz, VDAC1 cysteine residues: topology and function in channel activity and apoptosis, Biochem. J. 427 (2010) 445–454, http://dx.doi.org/10.1042/BJ20091690.
[43] S.R. Maurya, R. Mahalakshmi, Modulation of human mitochondrial voltage-dependent anion channel 2 (hVDAC-2) structural stability by cysteine-assisted barrel-lipid interactions, J. Biol. Chem. 288 (2013) 25584–25592, http://dx.doi.org/10.1074/jbc.M113.493692.
[44] S.R. Maurya, R. Mahalakshmi, Cysteine residues impact the stability and micelle interaction dynamics of the human mitochondrial β-barrel anion channel hVDAC-2, PLoS ONE 9 (2014), e92183, http://dx.doi.org/10.1371/journal.pone.0092183.
[45] P.J. Hogg, Disulfide bonds as switches for protein function, Trends Biochem. Sci. 28 (2003) 210–214, http://dx.doi.org/10.1016/S0968-0004(03)00057-4.
[46] J.I. Kourie, Interaction of reactive oxygen species with ion transport mechanisms, Am. J. Physiol. 275 (1998) C1–24.
[47] A. Messina, S. Reina, F. Guarino, A. Magrì, F. Tomasello, R.E. Clark, et al., Live cell interactome of the human voltage dependent anion channel 3 (VDAC3) revealed in HeLa cells by affinity purification tag technique, Mol. BioSyst. 10 (2014) 2134–2145, http://dx.doi.org/10.1039/c4mb00237g.
[48] C.M. Cremers, U. Jakob, Oxidant sensing by reversible disulfide bond formation, J. Biol. Chem. 288 (2013) 26489–26496, http://dx.doi.org/10.1074/jbc.R113.462929.
[49] A.V. Zima, L.A. Blatter, Redox regulation of cardiac calcium channels and transporters, Cardiovasc. Res. 71 (2006) 310–321, http://dx.doi.org/10.1016/j.cardiores.2006.02.019.